

Particle-In-Cell simulations of filamentation process in magnetized plasma of capacitively-coupled radio-frequency discharge

Huidong Huang¹ , Jian Chen¹  ‡, and Zhibin Wang¹ 

¹ Sino-French Institute of Nuclear Engineering and Technology, Sun Yat-Sen University, Zhuhai 519082, People's Republic of China

E-mail: chenjian5@mail.sysu.edu.cn

July 2024

Abstract. In the uniform radio-frequency capacitively-coupled plasma (RF-CCP) between a large electrode pair, adding an axial magnetic field induces diverse longitudinal filaments. This phenomenon, termed 'filamentation', challenges conventional understanding and remains poorly understood to date. To reveal its pattern dynamics, we conduct 2D Particle-In-Cell simulations to comprehensively examine whole process of filamentation, identifying two distinct stages. Initially, standing waves grows with a modulational instability, forming regular filaments. Subsequently, when initial wavenumber matching relation breaks, the plasma shifts towards dynamic regime governed by competition between Lorentz and thermal pressure forces, characterized by filaments' chaotic evolution. These novel clues pave the way to theoretically understanding the filamentation instability, and provides essential references in effectively manipulating the magnetized plasmas.

Keywords: pattern dynamics, radio-frequency capacitively-coupled plasma, Particle-In-Cell simulation

Submitted to: *Plasma Sources Sci. Technol.*

‡ Author to whom any correspondence should be addressed.

1. Introduction

Magnetic fields are commonly utilized in capacitively coupled plasma (CCP) discharges to enhance the plasma density [1–3] and modify plasma shape [4–6]. Experiments have demonstrated that CCPs subject to an axial magnetic field undergo filamentation, giving rise to a sequence of luminous patterns that extends along the magnetic field lines. These patterns can manifest either as organized formations (like concentric rings) or irregularly-moving filaments lacking regularity, showcasing diverse morphology that has captured extensive attention [7, 8]. Remarkably, this phenomenon provides, contrary to common belief [9], certain entrance into the bulk plasma for the surface RF disturbance despite lower frequency (e.g., 13.56 MHz [10–14]) compared to the plasma frequency (several gigahertz). Understanding the fundamental physics of the filamentation is imperative for effectively manipulating the magnetized plasmas, which plays a key role in various CCP techniques such as semiconductor etching [15, 16], surface modified [17] and material deposition [18].

For two decades, significant efforts have been devoted to experimental investigations of filamentary patterns. Konopka and Schwabe et al. carried out preliminary observations on the formation of luminous filaments [10, 11]. They proposed that the filamentation strength depends on the magnetization of ions, additionally their findings suggested that filamentation modifies dramatically the ion transport [11]. Thomas et al. expansively studied the filamentation in magnetized dusty plasmas [12, 13, 19, 20]. Through parameter sweep concerning magnetic intensity, power deposition, and gas pressure, they have given an empirical law of the filamentation strength. Recently, highly-resolving observation [14] has further identified several modes of micro-structure of filament, each occurring under varying experimental parameters. Results showed that each filament undergoes chaotic flowing and rotating ceaselessly. Overall, experiments over years have revealed increasing complexities, that is, non-linearities and unsteady non-equilibrium state, leaving behind a growing number of problems to be solved.

Besides the experiments, preliminary numerical studies have also been performed to explore the pattern dynamics in magnetized CCPs. Menati et al. employed a two-dimensional hybrid model to investigate

the pattern formation of in a magnetized capacitively coupled argon plasma for the configuration with a powered metal electrode and a grounded electrode with a dielectric barrier [21]. Simulation results showed the dielectricity is strongly correlated with the filamentation strength. Afterwards, a three-dimensional inertialess two-fluid model reproduced the longitudinal concentric stripes akin to experimental observation [22]. They recently progressed to making initial application of linearized fluid model in steady-state assumption and interpreted the pattern phenomenon as merely a higher-order diffusion mode [23], in omitting both intricacy of real electron dynamics and self-consistency of RF discharge [24].

Despite considerable endeavors, decisive theoretical breakthrough for explaining the filamentation is still absent. A central question that remains unsolved is *how magnetic fields facilitate the penetration of RF perturbations into the bulk plasma*. In addition, existing studies [11–14, 21, 22, 24] have never well unfolded the detailed process and non-linearities involved in pattern formation. Thus far, another physics question that remains unanswered is *what governs the pattern dynamics*. People have known very little about the dynamical processes involved in the formation and evolution of these patterns, which have impeded in-depth analysis.

The primary objective of our current work is to address the two major physics questions just posed. Given the inadequacy of available experimental facilities (e.g. International Micro-gravity Plasma Facility (IMPF) [10, 11], and Magnetized Dusty Plasma Experimental device (MDPX) [12, 13, 25].) in providing the mechanical data required for dynamic analysis, excellent functionality of Particle-In-Cell approaches [26–28] motivates our interest in launching kinetic simulations for reproducing entire process of filamentation.

In this paper, we conduct simulations of a magnetized argon RF-CCP by employing a Particle-In-Cell/Monte-Carlo-Collision (PIC/MCC) model [29–31]. This model incorporates the electron and ion kinetics as well as their collisions with the background gas [32, 33]. Our simulations comprehensively depict the kinetics involved in the whole process of filamentation. We identify two distinct stages therein, that is, firstly the stage of standing wave growing (SWG) and secondly the stage of pattern evolving (PE). During the SWG stage, regular plasma

filaments emerge from a uniform background until they reach saturation, providing clues for replying the first question. This stage reveals the presence of modulational instability (MI) [34–38]. In the PE stage, initially regular patterns undergo chaotic evolution, which addresses our second question. The forces governing the pattern dynamics are analyzed through fluid analysis.

This paper is organized as follows: the employed PIC/MCC model and the numerical settings are described in section 2. The simulation results are presented and discussed in section 3, and a summary is provided in section 4. Additional supports are presented in the appendix.

2. Simulation Model

In this study, we adopt a 2D rectangular simulation domain ($L_x \times L_y$) to simulate the filamentation process in magnetized CCPs, as sketched in figure 1. It should be noted that some experiments employed a more complex configuration (see IMPF reactor in figure A1 of Appendix A). We have performed a test simulation with IMPF-type configuration and the results show a similar pattern formation, justifying the adoption of the configuration in figure 1. In this paper, x and y signify separately the radial and axial coordinates respectively. The system lengths in x and y directions are denoted as $L_x = 9.9$ mm and $L_y = 14.8$ mm, respectively. The lower electrode located at $y = 0$ is powered with a radio-frequency voltage (sinusoidal waveform of amplitude $U_0 = 100$ V and working frequency $f_{RF} = 60$ MHz), and the upper electrode at $y = L_y$ is grounded. Particles that hit these two electrodes are assumed to be absorbed. The secondary electron emission [39] is disabled in the present work. This is justified by the fact that turning on the secondary electron emission has slight influence on the physical process and steady-state plasma parameters (see the results shown in figure A2 of Appendix A). Periodic boundary conditions are used for the left and right boundaries ($x = 0$ and $x = L_x$), as shown as vertical dashed lines in figure 1. A uniform magnetic field $|\mathbf{B}| = 1.0$ T is applied and aligned with the y axis. The domain is filled with argon as the background gas and only singly-charged Ar^+ are considered in the simulations. The heat map shows a typical spatial distribution of Ar^+ within the 2D simulation domain in current work.

All the simulations in this study are performed using a open-source PIC/MCC code named EDIPIC-2D. EDIPIC-2D has been well benchmarked against multiple codes [40] and has been successfully applied to numerous low-temperature plasma simulations, as recently reported in the literature [41–43].

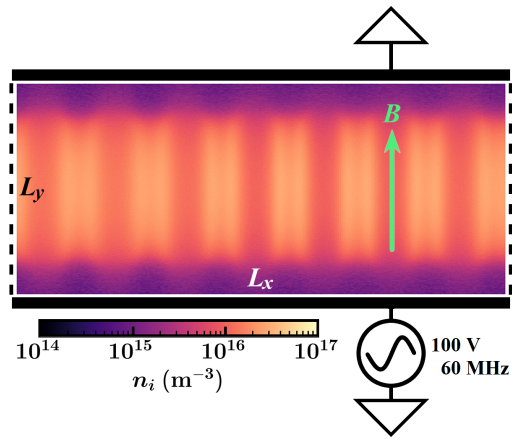


Figure 1. Schematic diagram of the setup.

To reduce the computational time of profile buildup process, the simulation starts with a uniform plasma with the plasma density $n_{p,0} = n_{e,0} = n_{i,0} = 2.5 \times 10^{16} \text{ m}^{-3}$, the electron temperature $T_{e,0} = 3.0$ eV and the ion temperature $T_{i,0} = 0.026$ eV. The background gas is argon and its pressure is fixed as 6.0 Pa. Initially, 500 super-particles per cell for each species are created, with the particle weight $w = 73728$. Three types of electron-neutral collisions, i.e. the elastic scattering, excitation and ionization, as well as the ion-neutral charge exchange collisions are included. The cross-section data used in the simulations are taken from [44–47]. The cell size $\Delta x = \Delta y = 38.4 \mu\text{m}$ is able to capture the Debye wavelength λ_{De} and the ion Larmor radius r_{Li} ($r_{Li} = 144 \mu\text{m}$ and λ_{De} are on the order of $10^2 \mu\text{m}$). Note that resolving electron Larmor radius ($130 \mu\text{m}$) requires a smaller cell size and leads to a unaffordable computation cost. Since the characteristic width of the filaments (1.4 mm) is much larger than the electron Larmor radius, we neglect the finite Larmor radius effects [48–50] on the filamentation process. The time step $\Delta t = 1.87$ ps is certain to resolve the electron plasma frequency $f_{pe} = 2840$ MHz as well as the radio-frequency $f_{RF} = 60$ MHz. To simulate the slow motion of filaments, the simulation was run for 1 ms (namely 530 million time steps). To capture the high frequencies physics, 24 probes are equidistantly arranged in 4 columns \times 6 rows at the bottom-left corner to record the time-dependent evolution of density, potential and electric field.

3. Simulation Results and Discussions

3.1. Standing Wave Growing Stage

Figure 2 shows the evolution of ion density distributions in standing wave growing stage, which is characterized by a standing wave arising from uniform background and growing until reaching saturation. Sub-

figures 2(a–c) depict the ion density distribution at 20 μs , 40 μs and 60 μs , while figures 2(d–f) show the corresponding ion density distribution along the mid-plane ($y=7.4$ mm, denoted by the white lines in figures 2(a–c)). As shown in figure 2(a), ion density keeps relatively uniform in the first 20 μs in the bulk region. Two RF sheaths are formed near the upper and lower electrodes with the thickness around 2 mm. The center plasma density is about $2 \times 10^{16} \text{ m}^{-3}$. Subsequently, radial disturbances surge from uniform background, leading to the density distribution with standing waveform, as depicted in figures 2(b) and 2(c). These standing waves maintain coherent structures that resembles the filaments observed in experiments [11, 13].

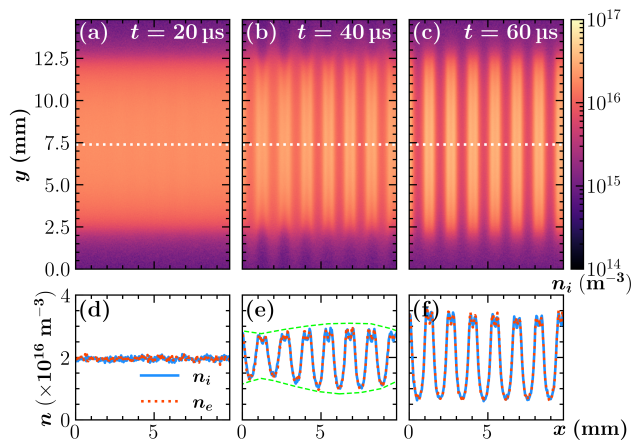


Figure 2. Standing wave growing stage. The Ar^+ 2D profiles present the plasma distribution at distinct moments: $t =$ (a) 20 μs , (b) 40 μs , (c) 60 μs . The white dot-dashed lines highlight the half-height altitude $y = 7.4$ mm. Blue and red curves indicating respectively Ar^+ and e^- depicted in (d–f) are their corresponding 1D profiles along the half-height slice. Typical modulational feature manifests on the spatial standing waveform in (e), which is enveloped by lime dashed curves.

As seen in figures 2(d–f), the amplitude of the standing wave keeps growing, during which quasi-neutral condition is still fulfilled (electron and ion densities are almost equal). More interestingly, as depicted in figures 2(e) and 2(f), the wave is clearly modulated, i.e. the amplitudes of crests and troughs at different locations are varied, exhibiting an envelope structure as a whole (denoted by the lime dashed curves). Though the wave itself is standing, the envelope is moving, forming a traveling wave packet. The occurrence of the wave packet signifies that the nonlinear effects come into play.

It should be noted that the observed standing wave differs from the trivial electromagnetic surface wave that propagates radially into the plasma because the electromagnetic wavelength is much larger than the radius of the calculation domain (see Appendix B). Instead, it is a type of electrostatic wave that occurs only when the axial magnetic field is applied.

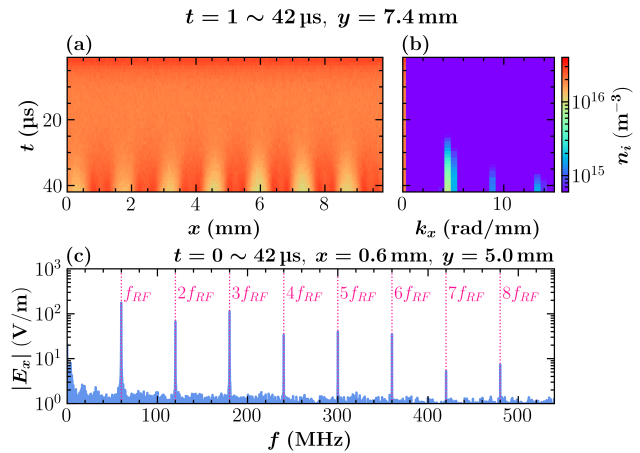


Figure 3. Wave characteristics of SWG stage. (a) shows the half-height slice of the density varying over time $t = 1 \sim 42$ μs , characterizing the SWG stage. And (b) is its wavenumber spectrum evolving over time. Frequency spectrum (c) records the temporal Fourier transform of radial electric field E_x , measured by a probe at position ($x = 0.6$ mm, $y = 5.0$ mm). The time window of sampling extends from 0 μs to 42 μs . The characteristic frequencies are numerically well matched to the RF wave and its higher harmonics.

To highlight the characteristics of the standing wave, we performed the Fast Fourier Transform to the radial electric field E_x . Figure 3(a) displays the ion number density evolution within the transformed time window $t = 1 \sim 42$ μs at the slice $y = 7.4$ mm, and figure 3(b) illustrates the corresponding wave number spectrum over time. The radial uniformity has been maintained until $t = 30$ μs , from which moment observable disturbances surge. Seven filaments form gradually with high regular shapes and nearly equal diameters. The radial wavelength of these wave packets is exact $\lambda_x = 1.4$ mm, i.e. $k_x = 2\pi/\lambda_x = 4.49 \text{ mm}^{-1}$, as depicted in figure 3(b). Figure 3(c) shows the spectrum of the horizontal component of \mathbf{E} at position ($x = 0.6$ mm, $y = 5.0$ mm), serving as a typical example. The frequency range spans from 0 MHz to 540 MHz. Result shows that the characteristic frequencies are exact $f_{RF} = 60$ MHz and its higher harmonics.

Multiple probes positioned at various locations are utilized to capture the temporal oscillations of filamentary plasma parameters during the SWG stage, encompassing densities, temperatures, velocities, current flux, electric potential, electrostatic field, among others. Our results show that these parameters share same characteristic frequency spectrum depicted in figure 3(c), regardless of probe location. These spectral profiles underscore the dominance of the wave directly induced by the RF pumping wave (with an RF supply working frequency $f_{RF} = 60$ MHz) along with its higher harmonics in driving the discharge. This result implies that the significance of cyclotron waves

and hybrid waves in this context is negligible, since plasma waves $f_{pe} \approx 1.2$ GHz and $f_{pi} \approx 4.6$ MHz, cyclotron waves $f_{ce} = 28$ GHz and $f_{ci} = 0.4$ MHz. Consequently, the standing wave is solely excited by RF pumping wave.

In current model, initially uniform plasma of 2D CCRF evolves between radially a pair of periodic boundaries and axially a pair of flat electrode. Both initial and geometric perturbations are excluded. It is thus quite different to the definite conditions of previous simulations [21, 22, 24]. The ion-particle fluid-electron hybrid scheme [51] employed in the work [21] adopted a axially non-symmetric 2D space to model the MDPX device [25, 52], which builds near both metal vertical sides the radial RF electric fields as a strong TW, namely a external perturbation. In contrast, our RF-TW is intrinsic. The two fluid model in works [22, 24] is performed in a 3D metal box space where over-simplistically omitting RF oscillatory supply, which yields a classical diffusion mode extending into three dimensions. It has produced also concentric filamentary patterns, since the steady-state theory permits the occurrence of higher-order diffusion mode. But it must to be pointed out that its physical basis is entirely different to our results. Our periodic boundaries never satisfies the boundary condition of a diffusion mode on the transverse direction.

In this situation, axial RF pumping should have produced merely a longitudinal wave (LW). For this reason, there should exist certain transverse wave (TW) mode to which permits the mode conversion from RF-LW. The wave mode in which the RF pumping engages is a theoretical challenge to determinate, since $f_{RF} = 60$ MHz differs far from frequency band of usual waves.

It is noteworthy that the radial standing wave generation is highly related to the axial magnetic field. The precise role of the strong magnetic field is complicated and requires a specific study. A rough explanation is that the magnetic field enables the energy transition from the pumping radio-frequency field to some plasma modes, akin to, for example, the generation of helicon waves [53–56].

Obvious wave modulation presents commonly in our results. It is usually linked to the occurrence of certain type of MI [57]. The assertion regarding the involvement of nonlinear wave-wave interaction in filamentation is further substantiated through the analysis of wave spectra. Within each frequency spectrum, as exemplified in figure 3(c), the characteristic frequencies are integer product of the base-frequency f_{RF} . A probable explanation is that the base-frequency f_{RF} wave beating primarily with itself, followed by nonlinear interactions between the RF wave and its higher harmonics, as well as amongst

the higher harmonics themselves. The mode matching process selects proper wavenumber and frequency. The temporal-spatial spectra should satisfy the energy conversion conditions, namely $f_1 + f_2 = f_3$ and $\mathbf{k}_1 + \mathbf{k}_2 = \mathbf{k}_3$, induced from the Manley-Rowe relations, according to the theory of wave non-linearity [58].

Drawing upon a synthesis of simulation outcomes and preceding discourse, a possible qualitative explanation for the filamentation mechanism emerges: the longitudinal RF wave, following mode conversion, infiltrates a transverse component of a specific wave. Facilitated by the mode matching mechanism, this wave manifests a characteristic spatiotemporal frequencies (f_{RF}, \mathbf{k}) . Subsequently, this RF transverse wave engenders modulational instability via nonlinear wave-wave interactions.

3.2. Pattern Evolving Stage

In the pattern evolving stage, the entire system undergoes turbulence since the end of the SWG stage. Bulk plasma transits to non-equilibrium dynamical system. The filaments can flow chaotically, merge in pairs or even surge suddenly from depletion region, suggesting their highly nonlinear nature. Regularity is disrupted as the number and positioning of filaments cease to remain constant, yet filaments maintain nearly equal diameters, and the saturation density limitation persists.

While the intricate trajectory of flow remains still unpredictable, an overarching trend emerges, driving the compression of filaments to coalesce into a system characterized by fewer number yet more pronounced amplitude of filaments. In our simulation, the equilibrated number of filaments hovers around four, yet a real steady-state never reached despite being quasi-steady in time-span of 0.1 ms.

At the microsecond scale, the bulk plasma distribution undergoes minimal changes, meaning that the temporal derivative of density $\partial_t n_s$ approaches zero. In the local conservation equation of charged species $s \in \{\text{Ar}^+, e^-\}$

$$\partial_t n_s + \nabla \cdot n_s \mathbf{U}_s = s_s, \quad (1)$$

the electron source s_e and ion source s_i are equal within bulk plasma. Moreover, source term s_s is equal to ionization rate $n_e \nu^{\text{ioniz}}$ where ν^{ioniz} is local ionization frequency. Computational results reveal that the ionization rate $n_e \nu^{\text{ioniz}}$ and the flux divergence $\nabla \cdot n_s \mathbf{U}_s$ are in comparable strength. This result indicates that the plasma is characterized by the relatively weak transport and the high local ionization efficiency, resulting in a high-density region. It can be observed that new plasma filament occasionally emerges from the depletion region, owing to the local high temperature and a weakened initial diffusion.

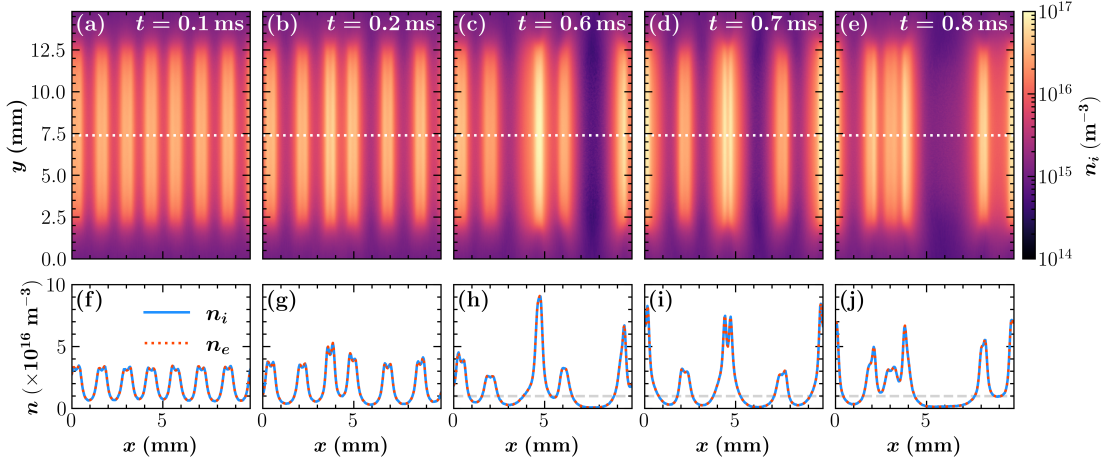


Figure 4. Pattern evolving stage. The Ar^+ 2D profiles present the plasma distribution at distinct moments: $t =$ (a) 100 μs , (b) 200 μs , (c) 600 μs , (c) 700 μs , (c) 800 μs . The white dot-dashed lines highlight the half-height altitude $y = 7.4$ mm. Blue and red curves indicating respectively Ar^+ and e^- depicted in (f–j) are their corresponding 1D profiles along the half-height slice. The grey dashed line in (h–j) is the density level of $1.0 \times 10^{16} \text{ m}^{-3}$, as a criterion to distinguish regions of filament or depletion.

Figure 4 shows the plasma distribution snapshots in the PE stage. Two groups of sub-figures 4(a–b) and sub-figures 4(c–e) present separately the transition from SWG to PE stage and a highly chaotic scenario. Their corresponding density curves are plotted in sub-figures 4(f–j) respectively. At 0.1 ms, seven filaments are regularly arranged (figure 4(a)) and their density peak are of equal height (figure 4(f)); But at 0.2 ms, only six irregular filaments distribute erratically (figure 4(b)), their density values start to differ as well (figure 4(g)). Such transition is attributed to the motion and pairwise merging of filaments. Having experienced a characteristic evolution time about 0.1 millisecond, a pair of filaments meld into single one, the charged particle numbers stack up, a brighter filament is left, as clearly drawn in figures 4(f–g). Next, the scenario projected onto figures 4(c–e) shows a representative instance of chaotic hydro-kinematics, depicted through the evolution of the ion distribution during time slot $t = 0.6 \sim 0.8$ ms, capturing various phenomena including chaotic flowing, pairwise merging, sudden emerging and wave saturating. At these moments, some packets flow together and locate close enough to dynamically view them as a whole. Density level $n_c = 1.0 \times 10^{16} \text{ m}^{-3}$ is thus introduced as a quantitative yardstick to divide the regions of filament and depletion. For instance, a connected area satisfying $n_i > n_c$ would be seen as a whole filament since it has concentrated majority of mass in the vicinity. To start, sub-figure 4(c) reveals five filaments, already exhibiting irregular positioning and varying magnitudes. Subsequently, as detailed in the dynamically evolving scenario presented in figure 5(a), the plasma mass gravitates towards the three filaments highlighted in figure 4(e) finally amidst the complete

chaos. A quintessential instance of “sudden emerging” manifests in figure 4(d), notably observed with the second filament from the right suddenly emerging from the depletion region at around 0.66 ms (See figure 5(a)). This occurrence unfolds abruptly and progresses swiftly, devoid of any discernible precursor indications at previous moment depicted in figure 4(c).

The complete fluid momentum balance equation for charged species consists of seven mechanical terms, namely, inertia $\partial_t m_s n_s \mathbf{U}_s$, convection $\mathbf{f}_s^{\text{conv}}$, stresses (both thermal pressure \mathbf{f}_s^{th} and viscosity $\mathbf{f}_s^{\text{visc}}$), collisions $\mathbf{f}_s^{\text{coll}}$, gravity \mathbf{f}_s^{gr} and electromagnetism \mathbf{f}_s^{em} , as referenced in the textbook [59] and literature [50, 60]. The momentum equation is thus

$$\partial_t m_s n_s \mathbf{U}_s = \mathbf{f}_s^{\text{conv}} + \mathbf{f}_s^{\text{th}} + \mathbf{f}_s^{\text{visc}} + \mathbf{f}_s^{\text{coll}} + \mathbf{f}_s^{\text{gr}} + \mathbf{f}_s^{\text{em}}, \quad (2)$$

where convection term is $\mathbf{f}_s^{\text{conv}} = -(\mathbf{U}_s \cdot \nabla) m_s n_s \mathbf{U}_s$, thermal pressure force is $\mathbf{f}_s^{\text{th}} = -k_B \nabla \cdot n_s \hat{\mathbf{T}}_s$, viscous force is $\mathbf{f}_s^{\text{visc}} = -\nabla \cdot \hat{\mathbf{\Pi}}_s$, gravitation is $\mathbf{f}_s^{\text{gr}} = m_s \mathbf{g}$ and Lorentz force is $\mathbf{f}_s^{\text{em}} = q_s n_s (\mathbf{E} + \mathbf{U}_s \times \mathbf{B})$. This fluid motion equation is introduced to discuss the hydrodynamics involving in non-equilibrium filaments. However, this universal formulation needs certain approximations for convenient determination. In the present scenario, gravitation never functions. The shear stress force predominantly originates from its gyroviscous component $\hat{\mathbf{\Pi}}_s^{\text{gyro}}$ [61], i.e. $\mathbf{f}_s^{\text{visc}} \approx \mathbf{f}_s^{\text{gyro}} = -\nabla \cdot \hat{\mathbf{\Pi}}_s^{\text{gyro}}$, with due consideration of the FLR effect [50, 62]. The formalism for numerical calculation of gyroviscosity tensor $\hat{\mathbf{\Pi}}_s^{\text{gyro}}$ ultimately adopted the widely used formulation outlined respectively in [50], consistent with that detailed in [43]. Notably, the majority of collisions in partly-ionized plasmas stem from the neutral collisions term, that is $\mathbf{f}_s^{\text{coll}} \approx \mathbf{f}_s^{\text{n}} = m_s n_s \nu^{\text{n-s}} \mathbf{U}_s$ with neutral collision frequency $\nu^{\text{n-s}}$ [23].

Slow dynamics of the patterns only concerns the time-averaged effects of RF plasma oscillations. We use angle brackets $\langle \rangle$ to denote the operator for time-averaging physical quantities over duration exceeding multiple RF periods, for instance, $\langle \square \rangle = \int_0^\tau \square dt$ as $\tau = 6T_{RF}^{-1} = 0.1 \mu\text{s}$. The time-averaged convection $\langle \mathbf{f}_s^{\text{conv}} \rangle$ is estimated by the ponderomotive force \mathbf{f}_s^{pm} i.e. $\langle \mathbf{f}_s^{\text{conv}} \rangle \approx \mathbf{f}_s^{\text{pm}}$, as substituting the plasma dispersion relation into the expression for the convective force $\langle \mathbf{f}_s^{\text{conv}} \rangle \approx -m_s n_s \nabla \langle \mathbf{U}_s^2 \rangle$ yields the expression for the electrostatic PM force $\mathbf{f}_s^{\text{pm}} = -\omega_{ps}^2 \nabla \langle \mathbf{E} \cdot \partial_\omega \hat{\epsilon} \cdot \mathbf{E} \rangle$ [63, 64]. Here, the plasma dielectric tensor $\hat{\epsilon} = \epsilon_0 [\mathbf{b} \otimes \mathbf{b} + (\hat{\mathbf{I}} - \mathbf{b} \otimes \mathbf{b}) / (1 - \omega_{cs}^2 / \omega^2)^2]$ is function of ω with the unit matrix $\hat{\mathbf{I}}$, the magnetic field direction unit vector \mathbf{b} and the cyclotron frequency ω_{cs} , and the plasma frequency $\omega_{ps} = \sqrt{\frac{n_s q_s^2}{\epsilon_0 m_s}}$ is circular frequency of Langmuir wave. The time-derivative term of the ponderomotive force [65–67] can be negligible in slowly varying RF-averaged waveforms. Contributions from anisotropic temperature [68] and non-local properties [69, 70] are disregarded. The time-averaged Lorentz force $\langle \mathbf{f}_s^{\text{em}} \rangle = q_s \langle n_s \rangle \langle \mathbf{E} + \mathbf{U}_s \times \mathbf{B} \rangle$ sees the time-averaged fields $\langle \mathbf{E} \rangle$ and $\langle \mathbf{U}_s \rangle$ where the high frequency oscillations are filtered out by time-averaging. Using the same method, we calculate the time-averaged values of thermal pressure force $\langle \mathbf{f}_s^{\text{th}} \rangle = -k_B \nabla \cdot \langle n_s \hat{\mathbf{T}}_s \rangle$, gyroviscous force $\langle \mathbf{f}_s^{\text{gyro}} \rangle = -\nabla \cdot \langle \hat{\mathbf{\Pi}}_s \rangle$, and neutral collisional friction $\langle \mathbf{f}_s^{\text{n}} \rangle = m_s \langle n_s \mathbf{U}_s \rangle \nu^{n-s}$. The time-averaged right-hand side of equation (2) is therefore

$$\mathbf{f}_s^{\text{tot}} = \mathbf{f}_s^{\text{pm}} + \langle \mathbf{f}_s^{\text{th}} \rangle + \langle \mathbf{f}_s^{\text{gyro}} \rangle + \langle \mathbf{f}_s^{\text{n}} \rangle + \langle \mathbf{f}_s^{\text{em}} \rangle, \quad (3)$$

where $\mathbf{f}_s^{\text{tot}}$ represents the total force experienced by the fluid on a microsecond time scale.

A numerical evaluation is conducted to compare the time-averaged contributions of five forces in equation (3), delving into the theoretically pertinent forces governing plasma manipulation along the radial axis. Our results indicate that the pattern dynamics in PE stage is primarily governed by time-averaged Lorentz force $\langle \mathbf{f}_s^{\text{em}} \rangle$ and time-averaged thermal pressure force $\langle \mathbf{f}_s^{\text{th}} \rangle$.

Figure 5 explores the relationship between the motion of filaments and the forces acting upon them. Figure 5(a) presents the patterns flowing and the total force direction. The spatiotemporal evolution graph displays the half-height slice of the ion density varying over time $t = 0.6 \sim 0.8$ ms (in the PE stage). This scenario has been projected its moments $t = 0.6, 0.7, 0.8$ ms onto figures 4(c–e). It presents a good sample delving into the chaotic hydro-kinematics of PE stage. Various phenomena including chaotic flowing, pairwise merging, sudden emerging and wave saturating are clearly captured here. White dot-dashed curves enclose the regions of ion density exceeding $1.0 \times 10^{16} \text{ m}^{-3}$ where are tagged as filament areas for

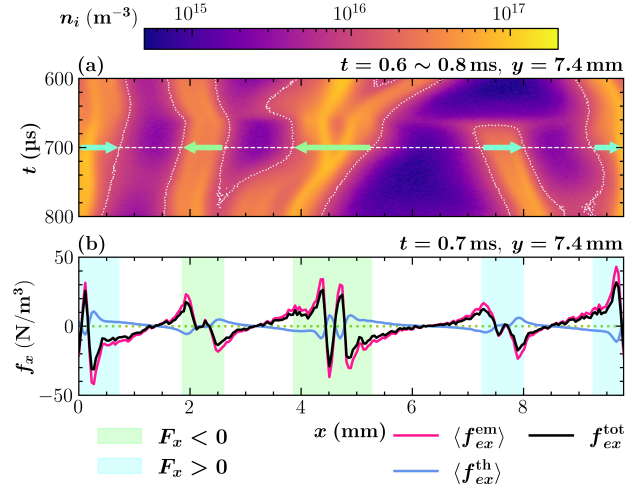


Figure 5. Fluid dynamics of PE stage. These half-height slices constitute (a) the Ar^+ density profile varying over time $t = 0.6 \sim 0.8$ ms, which displays the hydro-kinematics of PE stage. White dot-dashed contours close the regions of ion density exceeding $1.0 \times 10^{16} \text{ m}^{-3}$ where are viewed as plasma filaments. In (a), the rightward cyan or leftward lime arrow attached upon each filament indicates the direction of total force F_x acting on whole filament at the moment $700 \mu\text{s}$. (b) demonstrates the local volume force along the waistline $y = L_y/2$ at $700 \mu\text{s}$, including the resultant force (f_{ex}^{tot} , black curve) and two dominant forces, that is, the time-averaged Lorentz force ($\langle f_{ex}^{\text{em}} \rangle$, magenta curve) and the time-averaged thermal pressure force ($\langle f_{ex}^{\text{th}} \rangle$, azure curve) exerted upon electrons. In (b), lime or cyan patch spanning entire region of each filament, means that the total force acting on the whole filament is pointing to left-hand-side or right-hand-side, respectively.

the force calculation. Area total force F_x is defined by the filament area integral of the radial component of local total force $\mathbf{f}_e^{\text{tot}}$ acting on fluid electrons, namely, $F_x = \int_{\text{filament}} f_{ex}^{\text{tot}} dx dy$. If $F_x > 0$, it indicates that the total force is directed to the right, whereas if $F_x < 0$, it indicates that the force is directed to the left. The direction of resultant force acting on whole filament at moment $t = 0.7$ ms is indicated by the colored arrows overlaid on the heat map background. As illustrated in figure 5(a), the acceleration direction of filament areas is exactly coherent to the direction of the total force. Figure 5(b) displays the calculated result details of effective volume forces acting along the half-height level $y = L_y/2$ at the moment $t = 0.7$ ms. It includes the local total force (f_{ex}^{tot} , shown as the black curve) and two dominant forces: the time-averaged Lorentz force ($\langle f_{ex}^{\text{em}} \rangle$, represented by the magenta curve) and the time-averaged thermal pressure force ($\langle f_{ex}^{\text{th}} \rangle$, shown as the azure curve) acting upon electrons. In Besides, a lime or cyan patch spanning the entire region of each filament indicates that the area total force F_x acting on the whole filament is directed towards the left-hand side or right-hand side, respectively.

In the simulation results, at $t = 0.7$ ms, the plasma parameters along the half-height line are quasi-

stationary, exhibiting negligible changes within $\pm 1 \mu\text{s}$. Employing the average intensities of the five forces in the vicinity of $t = 0.7 \text{ ms}$, spanning 30 RF cycles (equivalent to $0.5 \mu\text{s}$), facilitates a straightforward comparison of the contributions of these five forces to the local plasma momentum change. The results reveal that these five forces are not balanced within the bulk plasma. In other words, the inertia term is always non-zero, which argues that the plasma of PE stage is far from a force-balanced system. The time-averaged thermal pressure force $\langle \mathbf{f}_s^{\text{th}} \rangle$ and the time-averaged Lorentz force $\langle \mathbf{f}_s^{\text{em}} \rangle$ significantly outweigh the other three forces (by three orders of intensity at least). Therefore, these two forces is sufficient to approximate the resultant force acting on the plasma. The thermal pressure force $\langle \mathbf{f}_s^{\text{th}} \rangle$ and the Lorentz force $\langle \mathbf{f}_s^{\text{em}} \rangle$ are oriented in the inverse direction locally, which eventually drives the particles towards higher-density areas. At larger scale, the sum of forces acting on each particle within the plasma filament is used to represent the resultant force acting on the entire filament, propelling the motion of the whole filament.

Despite the relative weakness of ponderomotive force \mathbf{f}_s^{pm} , the time-average term $\frac{\epsilon_0}{2} \langle E_x^2 \rangle$, representing radiation pressure, exhibits a steep gradient within the plasma bulk and also the electric field envelope appears akin to a solution of the nonlinear Schrödinger equation found within the set of Zakharov equations [37, 38, 71]. Generally, in steady-state plasmas described by Zakharov equations, the gradients of thermal and radiation pressures oppose each other [59, 72]. This implies that the PM effect tends exert pressure on the lower-density regions, while the thermal pressure force acts to smooth out density gradients. However, the radiation pressure does not match this relationship in our results; its spatial fluctuations align closely with the radial thermal pressure $k_B n_e T_{ex}$ throughout the domain. Hence, attempts to adapt the Zakharov equations to describe the filamentation are certain to fail.

4. Conclusions

In this study, we utilized 2D PIC/MCC simulations to investigate the filamentation process of CCRF magnetized plasma and analyze the associated pattern dynamics. We observed distinct stages in the process, delineating the Standing Wave Growing stage and the subsequent Pattern Evolving stage, with the moment of instability saturation marking a critical transition point. Initially, longitudinal filaments emerge from a uniform background, while in the Pattern Evolving stage, filaments can flow, grow, merge, and emerge suddenly from depletion regions.

Regarding wave characteristics, our results indi-

cate that the non-linear oscillations, of such as plasma and electrostatic field, exhibit waveform and spectrum properties of modulational instability in nonlinear wave theory. Self-modulation provides these characteristic spectra consisted of integer multiples of the base spatiotemporal frequencies. Though the exact wave mode remains unidentified, these findings partially reveal the instability mechanism.

Fluid mechanics reveals that time-integrated forces such as Lorentz and thermal pressure dominate during the Pattern Evolving stage. The competition between these two terms governs the motions of filaments. Additionally, results suggest that perturbed local ionization rate outweighs magnetic-confined radial diffusion, thereby facilitating sudden emergence of filament from a depletion region.

These novel clues offer valuable guidance for future investigations into pattern dynamics and essential reference for effective manipulations of industrial plasmas. The validation of wave non-linearity is waiting for future experimental measurement. Elucidating the intricacies of magnetic instability constitutes the forthcoming focal point of our future theoretical endeavors. Moreover, future research should include 3D kinetic simulations to explore filament micro-structures and extend investigations to electromagnetic cases.

Acknowledgments

We thank Prof. L. Xu , doctoral students J.-H. Chen and B.-M. Jin , for constructive sharing of thoughts. This work is supported by the National Natural Science Foundation of China (Grant Nos. 12305223, 12175322) and the National Natural Science Foundation of Guangdong Province (Grant No.2023A1515010762).

Appendix A. Supplemental cases

Authors have comprehensively analyzed the performance of argon plasma in different kinds of configurations. Plasma reactor models of varying size, different RF power supplies, effects of surface electron emissions (SEE) and varying axial magnetic field strength, have been compared. Two valuable supplemental cases are mentioned here to support our arguments. They are a case modeling IMPF type of reactor (see figure A1), and a case adding SEE effects (figure A2), separately.

Figure A1 presents a snapshot of n_e profile within the rectangle simulation with a IMPF-type reactor immersed in longitudinal external magnetic field $|\mathbf{B}| = 1.3 \text{ T}$, which has a size $23.2 \text{ mm} \times 11.6 \text{ mm}$. As mentioned in report [10], the CCRF reactor chamber of IMPF has a bottom RF electrode with grounded outer loop, separated by a thin gap, and a top grounded metal plate electrode. Sketched in figure A1, current

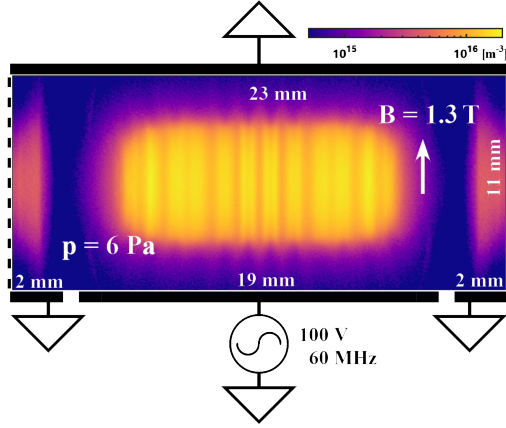


Figure A1. Case modeling IMPF reactor. A PIC simulation snapshot of the electron density profile of the filamentary magnetized plasma within a 23.2 mm \times 11.6 mm 2D rectangle CCRF discharge container, which opens a symmetric pair of 0.2-mm-wide vacuum cutout between 19.4-mm-wide inner RF electrode bottom edge and 1.8-mm-wide outer grounded metal bottom edges.

2D configuration setup opens a symmetric pair of 0.2-mm-wide vacuum cutout between 19.4-mm-wide inner RF electrode bottom edge and 1.8-mm-wide outer grounded metal bottom edges. Besides, the physic parameters are the same in section 2.

Despite a smaller simulation domain referring to the IMPF device, simulation produces the same filament patterns. The experimental observations show that the transversal sheath structures are formed over the vacuum gaps. Remarkably, the bright lumps near both sides are the transversal diffusion residues induced by the periodic boundaries rather than the uninterpretable modeling error. In comparison to the model illustrated in figure 1(a), the current reactor configuration is considered to introduce solely the RF alternating electric field above the vacuum gap, serving as a transverse perturbation pumping source. Initially, it was widely believed that this transverse RF electric field was the primary perturbation source leading to the filamentation phenomenon. Consequently, patterns were thought to originate from positions where the transverse RF field is strongest, i.e., the outer edge of the RF electrode [11, 21]. However, the simulation results indicate that the generation of filamentation does not depend on an externally applied transverse perturbation source, and the thermal perturbations alone are sufficient to elicit the instability.

Figure A2 encapsulates the simulation results incorporating the SEE effects. This case differs only in the engagement of secondary electron emissions. The other simulation parameters are the same in section 2. The effect of enabling SEE is to slightly increase the electron density on the surface of the metal electrode,

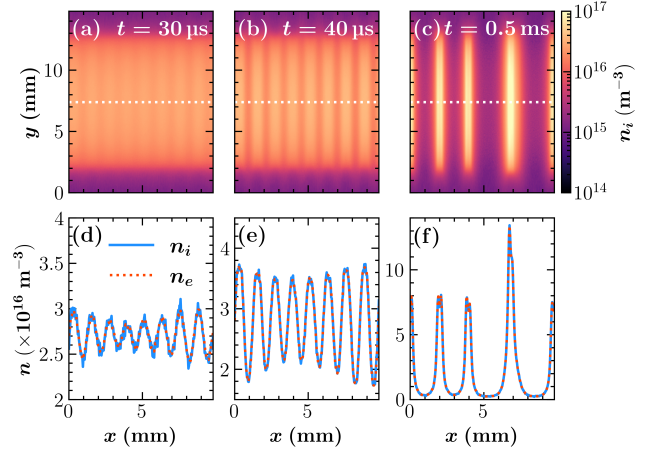


Figure A2. Case with SEE. Plasma population evolution within 500 microseconds. The Ar^+ 2D profiles present plasma distribution at distinct moments: $t =$ (a) 30 μs , (b) 40 μs , (c) 500 μs . The curves plotted in (d), (e) and (f) are the species density varying spatially along the waistline corresponding to (a–c), respectively. Typical modulational feature is presented upon the spatial waveform in (d) as well as (e).

thereby maintain the the quantity of charged particles. In the SWG stage (figures A2(d–e)), the mean plasma density at half-height level reaches $2.7 \times 10^{16} \text{ m}^{-3}$ (35% higher than mean density in figures 2(d–e)), however, the spatiotemporal distribution characteristics of the physical parameters in both sets of the cases remain consistent. The simulation extends over a time span of 0.5 ms, and the evolution trend of the total particle count within the simulated space closely approximates the curve depicted in figures 2 and 4. The filamentary pattern observed in the ion density distribution at three selected moments does not exhibit fundamental distinctions in general characteristics of the filamentation compared to the scenario without SEE effects. The density profile on the waistline vividly highlights the modulation of plasma waves. In summary, it can be concluded that the presence of SEE effects does not fundamentally impact the filamentation phenomena.

Appendix B. Discussions on common electromagnetic effects

At high frequencies, electromagnetic effects such as standing waves and skin effects can be observed, which cannot be described using the conventional electrostatic analysis. For a discharge with circular plates (radius R), the standing waves are due to a surface wave that propagates radially into the discharge [73]. But in current case, the standing wave effects are small, because the radical wavelength λ in the discharge plasma is much larger than the radius of the circular plate electrodes of IMPF

and MDPX, $R = 5$ or 8 cm respectively. $\lambda \approx \lambda_0 / \sqrt{1 + \min\{H, \delta_p\} / 4h_s} \gg R$, where $\lambda_0 = c / f_{RF} = 5$ m is the vacuum wavelength, $\delta_p \sim c / \omega_{pe}$ is the plasma skin depth, H is the bulk plasma thickness of a few centimeters and h_s is sheath thickness of a few millimeters. Skin effects are merely found at high densities where the plasma interior shields itself from the applied fields, and are negligible since the plasma skin depth $\delta_p \gg \sqrt{HR}$. These criteria are provided in the textbook [74].

References

- [1] Zheng B, Wang K, Grotjohn T, Schuelke T and Fan Q H 2019 *Plasma Sources Sci. Technol.* **28** 09LT03
- [2] Zhang Q Z, Sun J Y, Lu W Q, Schulze J, Guo Y Q and Wang Y N 2021 *Phys. Rev. E* **104** 045209
- [3] Patil S, Sharma S, Sengupta S, Sen A and Kaganovich I D 2022 *Phys. Rev. Research* **4** 013059
- [4] Barnat E V, Miller P A and Paterson A M 2008 *Plasma Sources Sci. Technol.* **17** 045005
- [5] Ma F F, Zhang Q Z, Cui Y M and Wang Y N 2023 *Appl. Phys. Lett.* **123** 202103
- [6] Dahiya S, Singh P, Das S, Sirse N and Karkari S K 2023 *Phys. Lett. A* **468** 128745
- [7] Melzer A, Krüger H, Maier D and Schütt S 2021 *Rev. Mod. Plasma Phys.* **5** 11
- [8] Tsankov T V, Chabert P and Czarnetzki U 2022 *Plasma Sources Sci. Technol.* **31** 084007
- [9] Conrads H and Schmidt M 2000 *Plasma Sources Sci. Technol.* **9** 441
- [10] Konopka U 2005 Complex plasmas in strong magnetic field environments *New Vistas in Dusty Plasmas (ICPDP vol 799)* (Orleans (France): AIP) pp 181–184
- [11] Schwabe M, Konopka U, Bandyopadhyay P and Morfill G E 2011 *Phys. Rev. Lett.* **106** 215004
- [12] Thomas E, Konopka U, Merlino R L and Rosenberg M 2016 *Phys. Plasmas* **23** 055701
- [13] Thomas E, Lynch B, Konopka U, Menati M, Williams S, Merlino R L and Rosenberg M 2019 *Plasma Phys. Control. Fusion* **62** 014006
- [14] Williams S, Chakraborty Thakur S, Menati M and Thomas E 2022 *Phys. Plasmas* **29** 012110
- [15] Cardinaud C, Peignon M C and Tessier P Y 2000 *Appl. Surf. Sci.* **164** 72–83
- [16] Wu B, Kumar A and Pamarthy S 2010 *J. Appl. Phys.* **108** 051101
- [17] Anders A 2005 *Surf. Coat. Technol.* **200** 1893–1906
- [18] Profijt H B, Potts S E, van de Sanden M C M and Kessels W M M 2011 *J. Vac. Sci. Technol. A* **29** 050801
- [19] Thomas E, Lynch B, Konopka U, Merlino R L and Rosenberg M 2015 *Phys. Plasmas* **22** 030701
- [20] Jung H, Greiner F, Piel A and Miloch W J 2018 *Phys. Plasmas* **25** 073703
- [21] Menati M, Thomas E and Kushner M J 2019 *Phys. Plasmas* **26** 063515
- [22] Menati M, Rasoolian B, Thomas E and Konopka U 2020 *Phys. Plasmas* **27** 022101
- [23] Chen F 2016 *Introduction to Plasma Physics and Controlled Fusion* 3rd ed (Cham: Springer International Publishing)
- [24] Menati M, Konopka U and Thomas Jr E 2021 *Contrib. Plasma Phys.* **61** e202100083
- [25] Thomas E, Merlino R L and Rosenberg M 2012 *Plasma Phys. Control. Fusion* **54** 124034
- [26] Birdsall C 1991 *IEEE Trans. Plasma Sci.* **19** 65–85
- [27] Verboncoeur J P 2005 *Plasma Phys. Control. Fusion* **47** A231
- [28] Arber T D, Bennett K, Brady C S, Lawrence-Douglas A, Ramsay M G, Sircombe N J, Gillies P, Evans R G, Schmitz H, Bell A R and Ridgers C P 2015 *Plasma Phys. Control. Fusion* **57** 113001
- [29] Vahedi V, DiPeso G, Birdsall C K, Lieberman M A and Rognlien T D 1993 *Plasma Sources Sci. Technol.* **2** 261–272
- [30] Donkó Z 2011 *Plasma Sources Sci. Technol.* **20** 024001
- [31] Wilczek S, Schulze J, Brinkmann R P, Donkó Z, Trieschmann J and Mussenbrock T 2020 *J. Appl. Phys.* **127** 181101
- [32] Vahedi V and Surendra M 1995 *Comput. Phys. Commun.* **87** 179–198
- [33] Tskhakaya D, Matyash K, Schneider R and Taccogna F 2007 *Contrib. Plasma Phys.* **47** 563–594
- [34] Nishikawa K 1968 *J. Phys. Soc. Jpn.* **24** 916–922
- [35] Nishikawa K 1968 *J. Phys. Soc. Jpn.* **24** 1152–1158
- [36] Zakharov V E, Musher S L and Rubenchik A M 1974 *JETP Lett.* **19** 151
- [37] Zakharov V E and Gelash A A 2013 *Phys. Rev. Lett.* **111** 054101
- [38] Gelash A A and Zakharov V E 2014 *Nonlinearity* **27** R1
- [39] Horváth B, Schulze J, Donkó Z and Derzsi A 2018 *J. Phys. D: Appl. Phys.* **51** 355204

- [40] Charoy T, Boeuf J P, Bourdon A, Carlsson J A, Chabert P, Cuenot B, Eremin D, Garrigues L, Hara K, Kaganovich I D, Powis A T, Smolyakov A, Sydorenko D, Tavant A, Vermorel O and Villafana W 2019 *Plasma Sources Sci. Technol.* **28** 105010
- [41] Janhunen S, Smolyakov A, Sydorenko D, Jimenez M, Kaganovich I D and Raitses Y 2018 *Phys. Plasmas* **25** 082308
- [42] Sun H, Chen J, Kaganovich I D, Khrabrov A and Sydorenko D 2022 *Phys. Rev. E* **106** 035203
- [43] Xu L, Sun H, Eremin D, Ganta S, Kaganovich I D, Bera K, Rauf S and Wu X 2023 *Plasma Sources Sci. Technol.* **32** 105012
- [44] Cramer W H 1959 *J. Chem. Phys.* **30** 641–642
- [45] Banks P 1966 *Planet. Space Sci.* **14** 1105–1122
- [46] Banks P 1966 *Planet. Space Sci.* **14** 1085–1103
- [47] Sakabe S and Izawa Y 1991 *At. Data. Nucl. Data Tables* **49** 257–314
- [48] Ramos J J 2005 *Phys. Plasmas* **12** 052102
- [49] Cerri S S, Henri P, Califano F, Del Sarto D, Faganello M and Pegoraro F 2013 *Phys. Plasmas* **20** 112112
- [50] Smolyakov A I, Chapurin O, Frias W, Koshkarov O, Romadanov I, Tang T, Umansky M, Raitses Y, Kaganovich I D and Lakhin V P 2017 *Plasma Phys. Control. Fusion* **59** 014041
- [51] Kushner M J 2009 *J. Phys. D: Appl. Phys.* **42** 194013
- [52] Thomas E, Konopka U, Artis D, Lynch B, Leblanc S, Adams S, Merlino R L and Rosenberg M 2015 *J. Plasma Phys.* **81** 345810206
- [53] Chen F F 1991 *Plasma Phys. Controlled Fusion* **33** 339
- [54] Chen F F and Arnush D 1997 *Phys. Plasma* **4** 3411–3421
- [55] Arnush D and Chen F F 1998 *Phys. Plasma* **5** 1239–1254
- [56] Chen F F 2015 *Plasma Sources Sci. Technol.* **24** 014001
- [57] Goldman M V 1984 *Rev. Mod. Phys.* **56** 709–735
- [58] Bellan P M 2006 *Fundamentals of Plasma Physics* 1st ed (Cambridge University Press)
- [59] Nicholson D R 1983 *Introduction to Plasma Theory* A Wiley Series in Plasma Physics (New York: Wiley)
- [60] Yang Y, Matthaeus W H, Parashar T N, Haggerty C C, Roytershteyn V, Daughton W, Wan M, Shi Y and Chen S 2017 *Phys. Plasmas* **24** 072306
- [61] Chew G F, Goldberger M L and Low F E 1956 *Proc. R. Soc. Lond. Ser. A.* **236** 112–118
- [62] Cheng C Z and Johnson J R 1999 *J. Geophys. Res. Space Physics* **104** 413–427
- [63] Maxwell J C 2010 *A Treatise on Electricity and Magnetism* 1st ed (Cambridge University Press)
- [64] Lundin R and Guglielmi A 2006 *Space Sci. Rev.* **127** 1–116
- [65] Washimi H and Karpman V I 1976 *JETP* **44** 528–531
- [66] Tskhakaya D D 1981 *J. Plasma Phys.* **25** 233–238
- [67] Kentwell G W and Jones D A 1987 *Phys. Rep.* **145** 319–403
- [68] Ghildyal V and Kalra G L 1998 *Phys. Plasmas* **5** 390–394
- [69] Smolyakov A I, Sydorenko D and Froese A 2007 *Plasma Phys. Control. Fusion* **49** A221
- [70] Iwata N and Kishimoto Y 2013 *Phys. Plasmas* **20** 083107
- [71] Zakharov V E 1972 *JETP* **35** 908–914
- [72] Treumann R A and Baumjohann W 1997 *Advanced Space Plasma Physics* (Imperial College Press)
- [73] Lieberman M A, Booth J P, Chabert P, Rax J M and Turner M M 2002 *Plasma Sources Sci. Technol.* **11** 283
- [74] Lieberman M A and Lichtenberg A J 2005 *Principles of Plasma Discharges and Materials Processing* 2nd ed (Hoboken, N.J: Wiley-Interscience)